Scripta Materialia 240 (2024) 115821

Contents lists available at ScienceDirect

Scripta Materialia

journal homepage: www.journals.elsevier.com/scripta-materialia

Universal function for grain boundary energies in bcc metals

Ooraphan Chirayutthanasak [a], Rajchawit Sarochawikasit [a,*], Sahachat Khongpia [b], Taira Okita [c], Somsak Dangtip [d], Gregory S. Rohrer [e], Sutatch Ratanaphan [a,b,f,*]

[a] Department of Computer Engineering, King Mongkut's University of Technology Thonburi, 126 Pracha Uthit Rd., Thung Khru, Bangkok 10140, Thailand
[b] Department of Tool and Materials Engineering, King Mongkut's University of Technology Thonburi, 126 Pracha Uthit Rd., Thung Khru, Bangkok 10140, Thailand
[c] Research into Artifacts, Center for Engineering, School of Engineering, the University of Tokyo, Tokyo, Japan
[d] Thailand Institute of Nuclear Technology, 9/9 Moo 7, Saimoon, Ongkharak, Nakhon Nayok 26120, Thailand
[e] Department of Materials Science and Engineering, Carnegie Mellon University, Pittsburgh, PA 15213-3890 USA
[f] Center of Excellence in Theoretical and Computational Science (TaCS-CoE), Faculty of Science, King Mongkut's University of Technology Thonburi (KMUTT), 126 Pracha Uthit Rd., Bang Mod, Thung Khru, Bangkok 10140, Thailand

ARTICLE INFO

Keywords:
Grain boundary energy
Anisotropy
Misorientation
Structure

ABSTRACT

Constructing microstructure-property-processing relationships in polycrystalline metals remains a challenge mainly due to the lack of quantitative relations between grain boundary (GB) energies and populations as well as the macroscopic properties associated with the processing dependent microstructure. Here, we present a universal function for computing the energies of arbitrary GBs in body-centered cubic (bcc) metals. The effectiveness of the universal function in describing the variations of the GB energies is demonstrated by consistency between the output of the function and the energies of ~ 2,500 GBs simulated by the embedded atom method. Large-scale comparisons between the interpolated energies and measured GB populations in W, Fe and ferritic steel reveal that the population distributions are governed by local energy minima located at the Σ1, Σ3, Σ9, Σ11, and Σ33a misorientations, representing a major step forward for the grain boundary engineering (GBE) of bcc metals.

Grain boundary engineering (GBE) has been widely used to optimize certain properties of polycrystalline materials including corrosion resistance, electrical conductivity, mechanical strength and ductility [1–10]. There remains a challenge in employing the GBE to tailor the grain boundary character distributions (GBCDs) for specific properties in body-centered cubic (bcc) metals. Although the properties of polycrystalline bcc metals can be enhanced by thermo-mechanical processes [1–4], the degrees of improvements associated with special or low-energy grain boundaries (GBs), such as Σ3, Σ9, and Σ27 are generally low compared with those observed for the face-centered cubic (fcc) metals [5–10]. Therefore, a complete list of the low-energy GBs in bcc metals, which might contribute to improve these properties, should be identified. Attempts to construct predictive models for calculating the GB energies for bcc metals have been reported previously [11–18]. For example, a lattice-matching model having only two fitting parameters successfully predicted the relative GB energies in Fe and Mo [18]. Nonetheless, consistencies between the GB energies determined from the lattice-matching model and atomistic simulations are rather low, especially for the low-angle or high-energy GBs, in which microscopic relaxations at the boundaries are generally observed [18]. An artificial neural network and Voronoi fundamental zone have been used to successfully predict the GB energies in iron, but their predictive errors especially for the low-energy GBs located in the proximities of energy cusps are rather high due to the non-uniform sampling and the noise in the iron data sets [11,12]. Furthermore, the multiple linear regression (MLR) model based on the cohesive energies and the Voigt-Reuss-Hill shear moduli has been used to predict the energies of 130 symmetric tilt GBs [13]. While the GB energies determined from the MLR model are comparable with the ones simulated by using density functional theory (DFT), there are some cases that the predicted energies are distinctively higher or lower than the DFT-simulated energies [13]. Based on the recent analysis of the DFT-simulated energies in relation to the cohesive energies, it was found that the GB energies can be solely described by using four geometric parameters and the universal GB energy model developed from these data sets can accurately predict the GB energies [16], highlighting the similarity of the GB energy landscape in isostructural bcc metals. It should be noted that the GB energies in Fe and Mo are linearly correlated [19] and the parametric constants defining the GB energy functions for Fe and W are also relatively comparable [14,15], indicating that the closed-form universal function for the GB

* Corresponding authors.
E-mail addresses: rajchawit.sar@mail.kmutt.ac.th (R. Sarochawikasit), sutatch.ratanaphan@mail.kmutt.ac.th (S. Ratanaphan).

https://doi.org/10.1016/j.scriptamat.2023.115821
Received 12 July 2023; Received in revised form 9 September 2023; Accepted 10 October 2023
Available online 21 October 2023

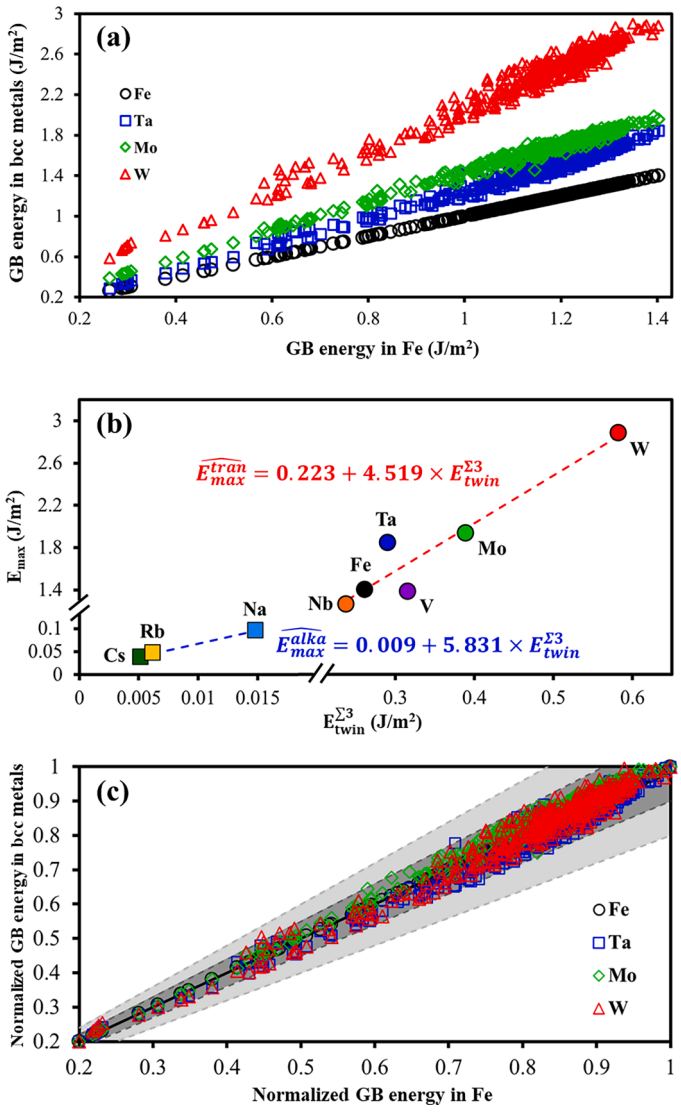

Fig. 1. **(a)** Relationships between the EAM-simulated GB energies in four bcc metals. Each point of data represents a GB with the same macroscopic structure and the coordinate is determined by the energy of the boundary in Fe and one of the other bcc metals: Fe (black), Ta (blue), Mo (green), and W (red). **(b)** Comparisons between the $E^{\Sigma3}_{twin}$ and E_{max} for the transition or alkali metals. **(c)** The GB energies normalized according to Eq. 1. Note that shaded regions in **(c)** represent the deviation from a unit slope (black dashed line) within 10% (dark grey) or 20% (light grey). (For interpretation of the references to color in this figure legend, the reader is referred to the web version of this article.)

energies in bcc metals might also require a small number of material dependent-parameters.

The goal of the current work is to produce a simple function that returns the energy of any GB in a bcc metal if the five parameters describing the bicrystal geometry are specified. To accomplish this, a function is fit to the calculated grain boundary energies of four bcc metals (Fe, Ta, Mo, and W) by using only two functional forms; Read–Shockley–Wolf (RSW) and parabolic functions, following methods similar to those originally developed by Bulatov et al. [20]. The generality of the function is then validated by comparing the predicted and calculated grain boundary energies in Nb, V, Na, Rb, and Cs. We employ large data sets of simulated GB energies, including previously simulated boundary energies (Fe, Mo, and W) [19,21] and additional boundary energies of Ta reported in the present study, to construct the universal function for GB energies in the isostructural bcc metals. Specifically, 408 GBs for each metal with 80 different misorientations and a range of GB orientations (tilt, twist, or mixed), were simulated by using embedded-atom method (EAM) potentials for Fe [22], Ta [23], Mo [24], W [25], implemented in the LAMMPS code [26] at 0 K. For each GB, 100 to 10,000 initial configurations with microscopic displacements of atoms at the boundaries are generated using an approach described in our previous studies in order to improve the search for the global minimum energy [19,21]. The GB energy is then obtained from the lowest value among the minimized energies of the initial configurations. As shown in Fig. 1a, the EAM-simulated GB energies for Fe, Mo, Ta, and W, having the cohesive energies (E_{coh}) of 4.12, 6.82, 8.09, and 8.76 eV/atom, respectively, are linearly correlated. The implication of these results is that the variations of GB energies in isostructural bcc metals could be modeled by using an appropriate scaling factor.

To normalize the grain boundary energies in Fig. 1a, the minimum and maximum grain boundary energies for each metal are selected as parameters. In each case, the minimum is the energy of the Σ3 {112} twin boundary ($E^{\Sigma3}_{twin}$). Because the energy of Σ23 {310} twist ($E^{\Sigma23}_{max}$), which is either the highest energy GB or within 98.5 % of the highest energy GB for Fe, Mo, Ta, and W (see Fig. 1b or supplementary data), is linearly correlated with the coherent twin boundary energy ($E^{\Sigma3}_{twin}$), the grain boundary with the maximum energy (E_{max}) for the transition metals is then determined from a trend line: $\widehat{E^{tran}_{max}} = 0.223 + 4.519 \times E^{\Sigma3}_{twin}$. The value of $E^{\Sigma23}_{max}$ in Na, Rb, and Cs is also linearly correlated with the $E^{\Sigma3}_{twin}$, but the trend line for these alkali metals is significantly different: $\widehat{E^{alka}_{max}} = 0.009 + 5.831 \times E^{\Sigma3}_{twin}$, primarily due to its electron configuration having only a single valence electron, reducing the strength of the metallic bonding, melting points, and elastic constants compared to the transition metals [22–25,27–29].

To normalize the energies so that the maximum energy is 1.0, we note that the ratio of $E^{\Sigma3}_{twin}$ to E_{max} is approximately 0.2 for all bcc metals. This leads to the simple linear expression in Eq. 1 to determine the normalized grain boundary energy (E^{norm}_{GB}) from the computed energy (E_{GB}).

$$E^{norm}_{GB} = 0.2 + 0.8 \times \left(\frac{E_{GB} - E^{\Sigma3}_{twin}}{E_{max} - E^{\Sigma3}_{twin}} \right) \quad (1)$$

The computed grain boundary energies for Fe, Mo, Ta, and W, normalized by Eq. 1, are compared in Fig. 1c. This comparison shows that nearly all of the grain boundaries have normalized energies that deviate from ideal linear scaling by less than 10 %.

With the computed GB energies normalized in this way, we can fit a piecewise continuous Read–Shockley–Wolf (RSW) function so that we can estimate the energy of any boundary by interpolation [14,15,20,30]. To do this, we use a method that is similar to that originally developed by Bulatov et al. [20]. Particularly, the normalized energies are first categorized into three scaffolding subsets according to their rotation axes: <100>, <110>, and <111>. For example, the scaffolding subsets of the GB energies with the <100> rotation axis are shown in Fig. 2. The unknown energy of a given symmetric tilt (Fig. 2a) or twist GBs (Fig. 2b) located at a misorientation angle (θ) in close proximity to the simulated energies is interpolated from Eq. 2:

$$f_{rsw}(x,\ a) = \sin\left(\frac{\pi x}{2}\right)\left[1 - a\log\sin\left(\frac{\pi x}{2}\right)\right],\ \text{where } x = \frac{\theta - \theta_{min}}{\theta_{max} - \theta_{min}}. \quad (2)$$

A shape parameter (a) is fit to the data and equal to 0.5 for most boundaries, but for the cases of the <110> symmetric tilt, <110> and <111> twist boundaries, the best fit values of $a^{tilt}_{110} = 0.70$, $a^{twist}_{110} = 0.46$, and $a^{twist}_{111} = 1.00$ were used. For all tilt GBs with <100> rotation axis as shown in Fig. 2c, the energies of asymmetric boundaries are interpolated from the symmetric tilt boundary energies that were previously described by the RSW function.

The comparison between the simulated and interpolated GB energies in Fig. 2d indicates that the universal function is satisfactory for predicting the grain boundary energies in the four bcc metals. The

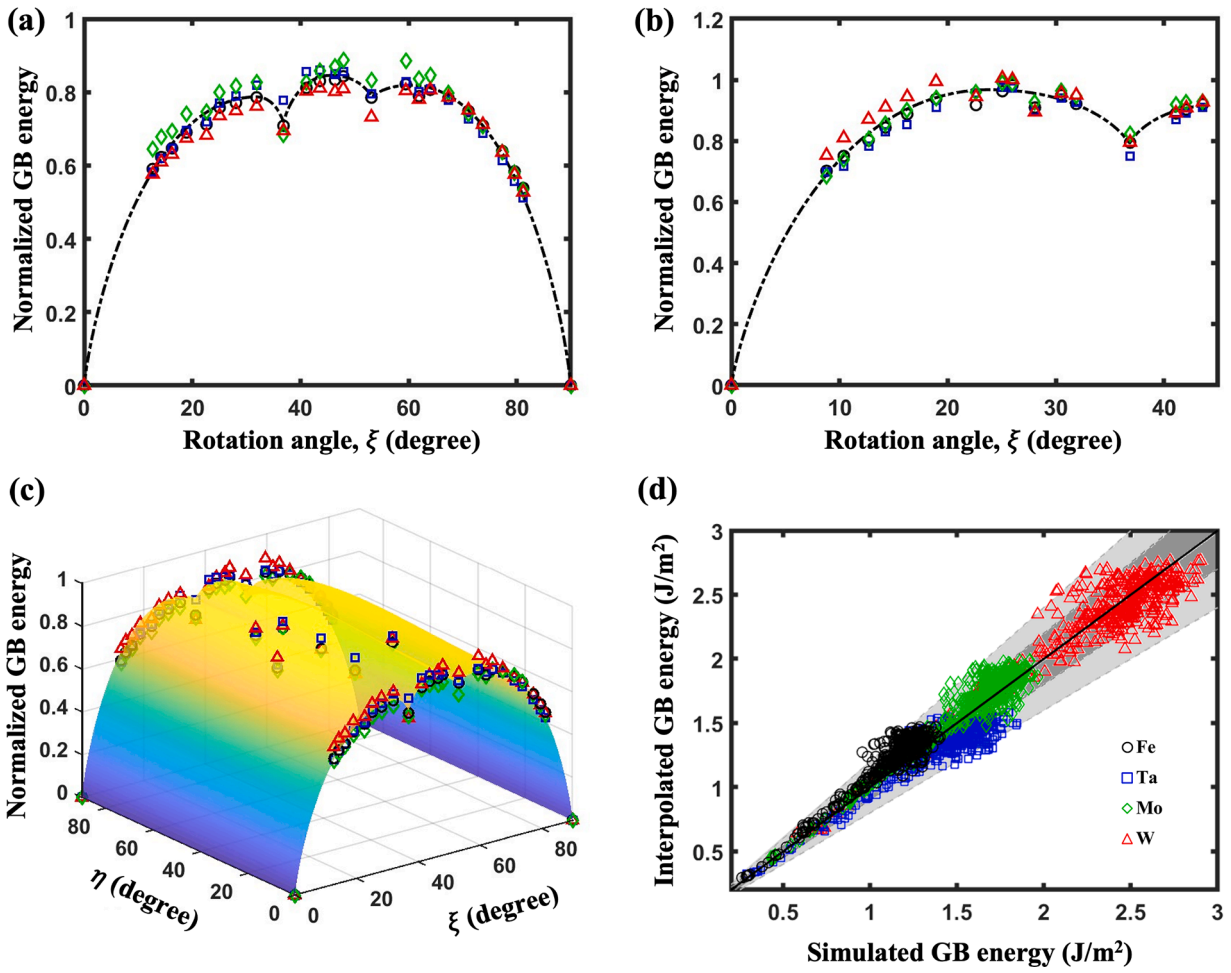

Fig. 2. The energies of **(a)** symmetric tilt, **(b)** pure twist and **(c)** all tilt GBs for <100> rotation axis, plotted by using the normalized scheme and subsequently fitted with the interpolation functions. **(d)** Comparisons between the EAM-simulated GB energies and the energies of the same boundaries interpolated from the GB energy function. Note that each point of data in **(d)** represents the GB energy in Fe (black), Ta (blue), Mo (green), or W (red) and shaded regions represent the deviation from a unit slope (black dashed line) within 10% (dark grey) or 20% (light grey). (For interpretation of the references to color in this figure legend, the reader is referred to the web version of this article.)

correlation coefficient between the interpolated and simulated energies is 0.94 and the root mean square error is 0.051 J/m^2. While there is some scatter, 90 % of the interpolated energies differ from the computed values by less than 10 % and only 1% differ from the computed value by more than 20 %. This is accomplished with only a single element specific parameter, $E_{twin}^{\Sigma 3}$, in the universal function. All simulated and interpolated energies as well as the MATLAB scripts used to compute the energy function have been made available in supplementary data or at the GitHub repository (https://github.com/simdsci/uGBE_BCC).

To determine if the function can determine the grain boundary energies of metals not involved in the normalization and fitting process, we have computed the energies of 408 grain boundaries in Nb [27] and Na [28] and 10 GBs in V [34], Rb [29], and Cs [29] using atomistic simulations with EAM potentials. The 408 GBs in Nb and Na are the same ones examined for Fe, Mo, W, and Ta. The 10 GBs in Fe, Ta, Mo, W, V, Nb, Na, Rb, and Cs were six symmetric tilt (Σ3 {111}, Σ3 {112}, Σ5 {012}, Σ5 {013}, Σ7 {123}, and Σ9 {122}), four twist GBs (Σ3 {110}, Σ5 {100}, Σ7 {111}, and Σ9 {110}); this subset was selected to facilitate a comparison to published energies obtained from DFT calculations [13]. Additionally, the DFT-simulated energies of symmetric tilt GBs: Σ3 {111}, Σ3 {112}, Σ9 {114}, Σ11 {113}, Σ11 {233}, Σ17 {223}, Σ17 {334}, Σ19 {116}, and Σ19 {133} in Fe, Mo, W, Ta, Nb, and V [31,32], were included in the comparisons. Furthermore, the recent DFT-simulated energies of symmetric tilt GBs in W [33] with low Σ (Σ5 {012}, Σ5 {013}, Σ9 {114}, and Σ11 {113}) and relatively high Σ (Σ13 {023}, Σ17 {014}, Σ17 {334}, Σ27 {255}, Σ33 {118}, and Σ43 {335}), were also considered.

Fig. 3 shows point-by-point comparisons between the EAM-simulated, DFT-simulated, and interpolated GB energies in the bcc metals. While Fig. 3a shows that there is some scatter with respect to a perfect fit for the 10 high symmetry GBs in Fe, Ta, Mo, W, Nb, V, Na, Rb, and Cs, the EAM and the DFT-simulated GB energies by Zheng et al. [13] are strongly correlated as reflected by the correlation coefficients (C_{EAM}^{DFT}= 0.96) and root mean square error of (RMSE= 0.28 J/m^2). Because of the computationally intensive calculations, the DFT-simulated GB energies are obtained from the fully-relaxed GB structure of Mo [13]. Consistency between the EAM and the DFT-simulated GB energies are observed for Mo but not in the cases of the Fe, in which GB structures and energies are substantially influenced by magnetism [19,35,36]. In other words, the large number of initial structures employed for the EAM-simulated GB could provide a better scheme to find the global lowest energy GB compared with the high-throughput DFT calculations [13], resulting in DFT-simulated GB energies that are generally higher than those determined from the EAM simulations. For the GBs with either low symmetry or high Σ, the DFT-simulated energies for each bcc metal [31–33] are almost perfectly correlated with the EAM-simulated GB energies (C_{EAM}^{DFT}= 0.97 and RMSE= 0.092 J/m^2). Although there are differences between some of

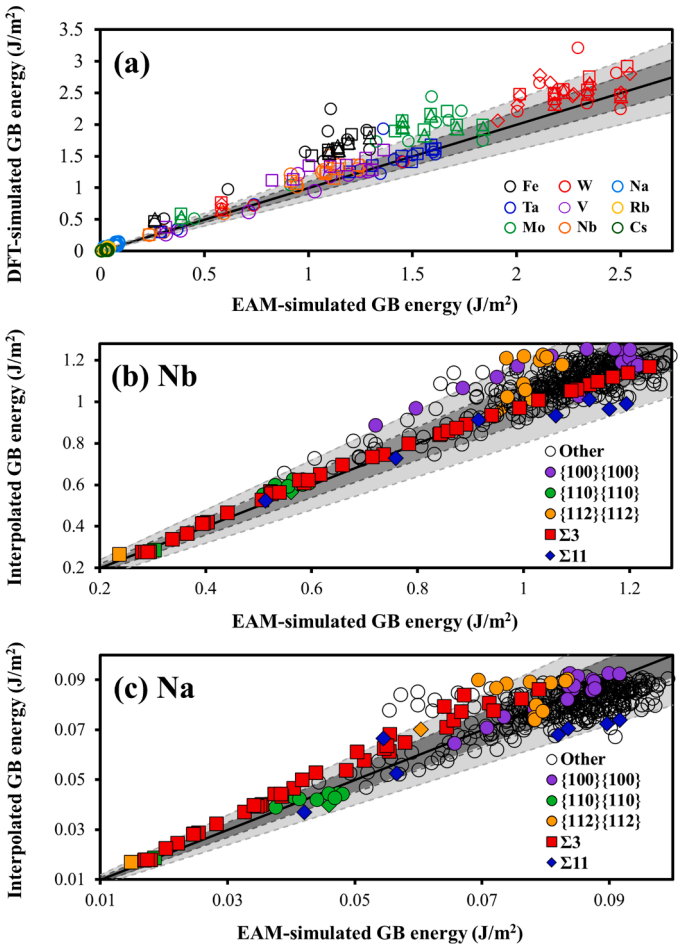

Fig. 3. **(a)** Comparisons between the EAM and DFT-simulated GB energies by Zheng et al. [13] (circles), Li et al. [31] (squares), Scheiber et al. [32] (triangles), and Zheng et al. [33] (squares). Each point of data represents a GB energy in Fe (black), Ta (blue), Mo (green), W (red), V(purple), Nb (pink), Na (light blue), Rb (yellow), and Cs (dark green). Comparisons between the EAM-simulated GB energies and the energies of the same boundaries interpolated from the GB energy function for **(b)** Nb and **(c)** Na. The data are classified into six groups: Σ3 (red squares), Σ11 (blue diamonds), {100}{100} (purple), {112}{112} (orange), {345}{345} (green), and the other GBs (black circles). Note that shaded regions represent the deviation from a perfect fit having a unit slope (black line) within 10% (dark grey) or 20% (light grey). (For interpretation of the references to color in this figure legend, the reader is referred to the web version of this article.)

the EAM and DFT calculated energies, the fact that the majority of the values differ by less than the estimated 10% error in the EAM calculations [37] and the overall strong correlation with the DFT energies indicates that the calculated results here are consistent with the previous results [13]. It was found that for Fe and Cr, magnetic contributions led to differences between the DFT-simulated and EAM simulated GB energies [31]. Therefore, the function may be applied to the other bcc structured materials, but the accuracy of the interpolated GB energies might suffer from unconsidered magnetic contributions to the energy, compared with the ones of Fe, Ta, Mo, and W.

Fig. 3b shows comparisons between the EAM-simulated and interpolated energies of 408 GBs in Nb. Interestingly, the interpolated and simulated energies are strongly correlated for the GBs having energies less than 0.5 E_{max}, as indicated by the correlation coefficient of 0.98. Although, the degree of correlation depends on the range of GB energy considered, deviations from a perfect fit with a unit slope are generally less 20%, excepted in the cases of the high-energy boundaries having symmetric GB with {100}, {112}, and {345} orientations. Similar agreements between the EAM-simulated and interpolated energies are also observed in Na (Fig. 3c), but the interpolated energies clearly deviate from the trend line particularly for the interpolated energies greater than 0.06 J/m^2. Because the energies of asymmetric or mixed GBs are interpolated from the three scaffolding subsets with the <100>, <110>, and <111> rotation axes, strong consistencies between the EAM-simulated and interpolated energies are generally observed for the tilt GBs, Σ3, or Σ11 but not for the asymmetric or mixed (other) GBs, in which the accumulation of interpolation errors results in the discrepancies or worst-behaving boundaries for the other GBs in Fig. 3b or Fig. 3c. The energy of the Σ23 {310} twist GB, E_{max}= 0.096 J/m^2 is lower than the actual maximum GB energy located at Σ49 {11 5 1}{11 5 1} 0.099 (**supplementary data**), leading to the slightly lower correlation coefficient of 0.94 for the GBs having energies less than 0.5 E_{max} compared with those observed in Nb. The increased accuracy of the interpolation function at lower relative grain boundary energies has implications for grain boundary engineering. Lower energy grain boundaries (those with energies less than 0.5 E_{max}) are hypothesized to contribute to improvements in the properties of bcc metals [38] and have relatively higher populations than higher energy grain boundaries [14,15,21]. We use the relationship between energy and population to compare the interpolated energies to experiments. We compare 39,554 interpolated energies that span the five macroscopic degrees of freedom (**supplementary data**) to measured grain boundary populations in three isostructural bcc metals (Fe [39], W [40], and ferritic steel [41]).

Fig. 4 compares the normalized energies and the measured populations for the symmetric tilt and pure twist GBs with <100>, <110>, and <111> axes. Although the measured GB populations are noticeably different, the variation of GB populations are all inversely correlated with their energies especially at the low angle grain boundaries (LAGBs or Σ1) and other local minima in the energy. In particular, the populations of LAGBs are generally higher than the rest of the GBs except for the case of symmetric tilt GBs with the <110> axis or twist GBs with the <110> axis, in which the maximum population is centered around the Σ3 {211} symmetric tilt (coherent twin) GB in the ferritic steel, as shown in Fig. 4b and Fig. 4e, respectively. These inverse relationships offer indirect validations of the GB energies, similar to what have been observed for fcc metals [42]. Interestingly, Homer et al. [43], found that machine learning trained on small data sets of LAGBs performed well on the prediction of all high angle grain boundaries (HAGBs). Therefore, the insight on the geometry and topography of the GB energies as well as the inverse relationships in the bcc metals reduce the number of GB energies that are needed to construct the GB energy function [14]. Because the energy cusp at the Σ3 coherent twin is much lower than those at the other symmetric tilt (Σ5{310}, Σ5{210}, Σ11{332}) or twist GBs (Σ5{100}, and Σ11{110}), the populations for these GBs (whose energies are > 0.5 E_{max}) are infrequently observed (see Fig. 4a, Fig. 4b, Fig. 4d, and Fig. 4e, respectively).

Fig. 5 shows comparisons between the normalized GB energies and populations for four misorientations that have local minima in the GB energy less than 0.5 E_{max} (Σ3, Σ9, Σ11, and Σ33a). The populations of boundaries with misorientations with higher grain boundary energies (for example, Σ5 and Σ7) are not correlated to the population. For the Σ3 misorientation as shown in Fig. 5a, the most commonly observed GBs correspond to low-energy GBs, regardless of the differences in the material syntheses, mechanical treatments, and annealing parameters in Fe [39], W [40], and ferritic steel [41]. The expected inverse relationship between population and energy is clearly observed for the Σ9, Σ11, and Σ33a misorientations; all of these misorientations have certain grain boundary plane orientations with energies that are less than 0.5E_{max}.

The results in Fig. 5 show that when a misorientation has grain boundary plane orientations with energies that are less than 0.5 E_{max}, there is a significant effect on the grain boundary population, magnifying the relative population of the lowest energy grain boundaries with respect to the higher energy boundaries. These boundaries, which include Σ1 (LAGBs), Σ3, Σ9, Σ11, and Σ33a misorientations play a significant role for the microstructure-processing-property relationships, and thus these low-energy GBs, which can be considered special with respect to their energy distributions, should be included for the quantitative descriptions of the GBE of bcc metals.

It was recently demonstrated that the energies of symmetric GB (Σ3 {111}, Σ3 {112}, Σ5 {013}, and Σ9 {114}) at high-temperatures in W [44] can be well predicted up to 0.55 of its melting temperature (T_m) by using only a temperature-dependent elastic modulus (c_{44}), which is independent of the GB [45]. Additionally, the fact that the variation of GB populations in Fe annealed at 550 °C (0.46T_m) for 16 hours [39] are inversely correlated with their energies (see Fig. 4 and Fig. 5), it is reasonable to speculate that the relative GB energies at the high temperature are similar to those produced by the universal function or the atomistic simulations at 0 K. Furthermore, given that the composition of the ferritic steel 0.04 C–1.52 Mn–0.2 Si–0.22 Mo–0.08 Ti–0.033 Al (wt. %) [41], was rather complex, if the segregation of trace impurities caused significant changes to the GB energies, this would be evident in changes to the GBCD. Nevertheless, the relationships between the GB energies and populations in the Fe and ferritic steel are relatively comparable as shown in Fig. 4 and Fig. 5, indicating that solute segregation in the ferritic steel does not lead to sweeping changes in the shape of the grain boundary energy function, consistent to what have been observed for the austenitic steel [46,47]. However, when solute segregation or complexion transitions lead to changes in the grain boundary energy landscape, as has been documented in the past, [48–51], the GB energy function's predictions will have limited accuracy.

The successful development of a single function to describe the energies of GBs for isostructural metals suggests that the geometry of the atomic basis of a crystal structure is more important for determining the distribution of GB energies than the chemical identity of the metallic atoms. If this is true for other crystal structures, and there is evidence that it is true for fcc metals [52], it would greatly simplify the task of cataloging the grain boundary energies for materials. If similar scaling laws existed for other GB properties of isostructural materials (for example, mobility), they would be equally valuable.

In summary, the GB energy function for bcc metals was developed based on the simulated GB energies of Fe, Ta, Mo, and W and then validated by comparisons to calculated grain boundary energies of Ta, Nb, V, Na, Rb, and Cs. The simulated GB energies are scaled by the energy of Σ3 coherent twin ($E_{twin}^{\Sigma 3}$) in each metal, revealing an isostructural grain boundary energy distribution in the bcc metals. Consequently, to fully describe variations of GB energies across the entire GB space, only a single element-specific parameter ($E_{twin}^{\Sigma 3}$) is required to accurately describe the energies of arbitrary GBs in a given bcc metal. Isostructural relationships between the GB energies and populations in bcc metals (W, Fe, and ferritic steel) are observed for misorientations that have low energy boundaries, including Σ1, Σ3, Σ9, and Σ11, representing a potential new type of special GB that might be

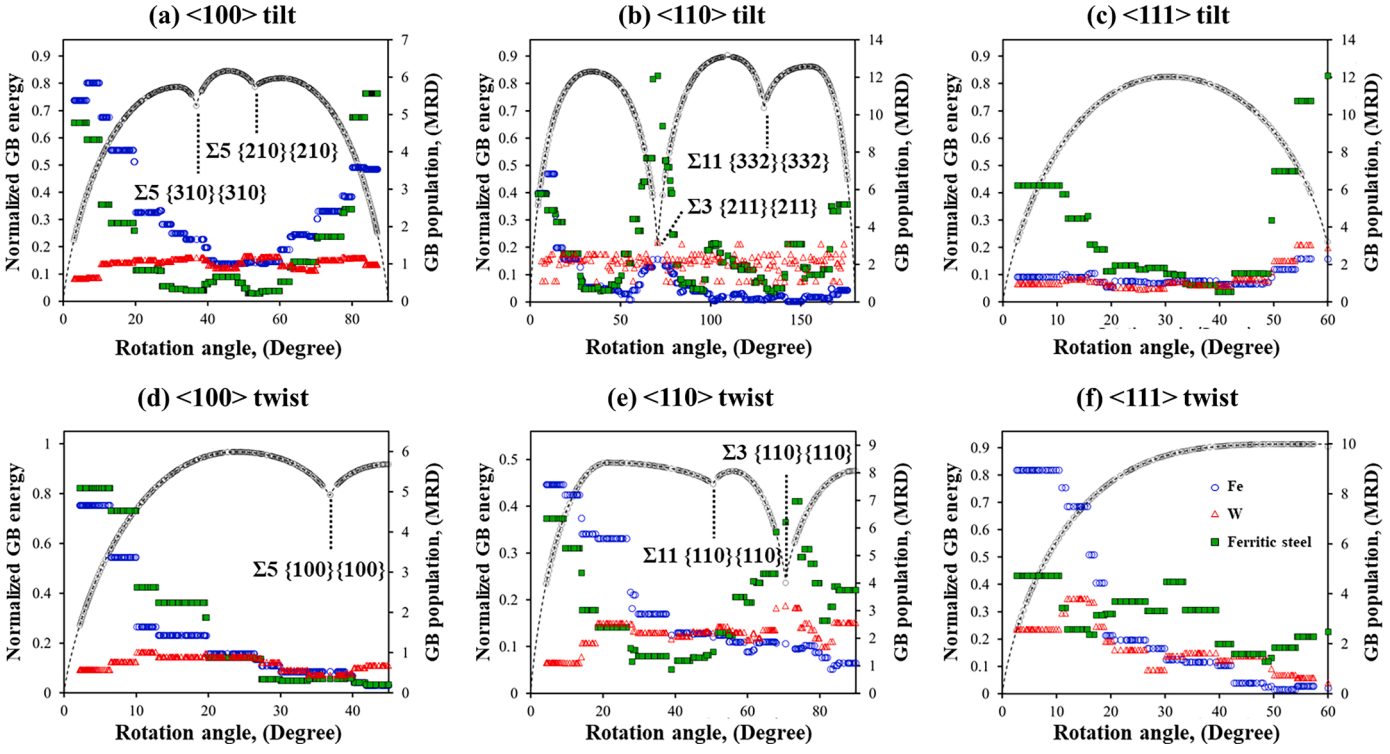

Fig. 4. Comparisons between the normalized GBs energies (black circles) determined from the GB energy function and the measured GB populations, plotted in units of multiples of a random distribution (MRD), in Fe [39] (blue circles), W [40] (red triangles), and ferritic steel [41] (green squares) for the symmetric tilt and pure twist GBs with <100>, <110>, and <111> axes. (For interpretation ofthe references to color in this figure legend, the reader is referred to the web version of this article.)

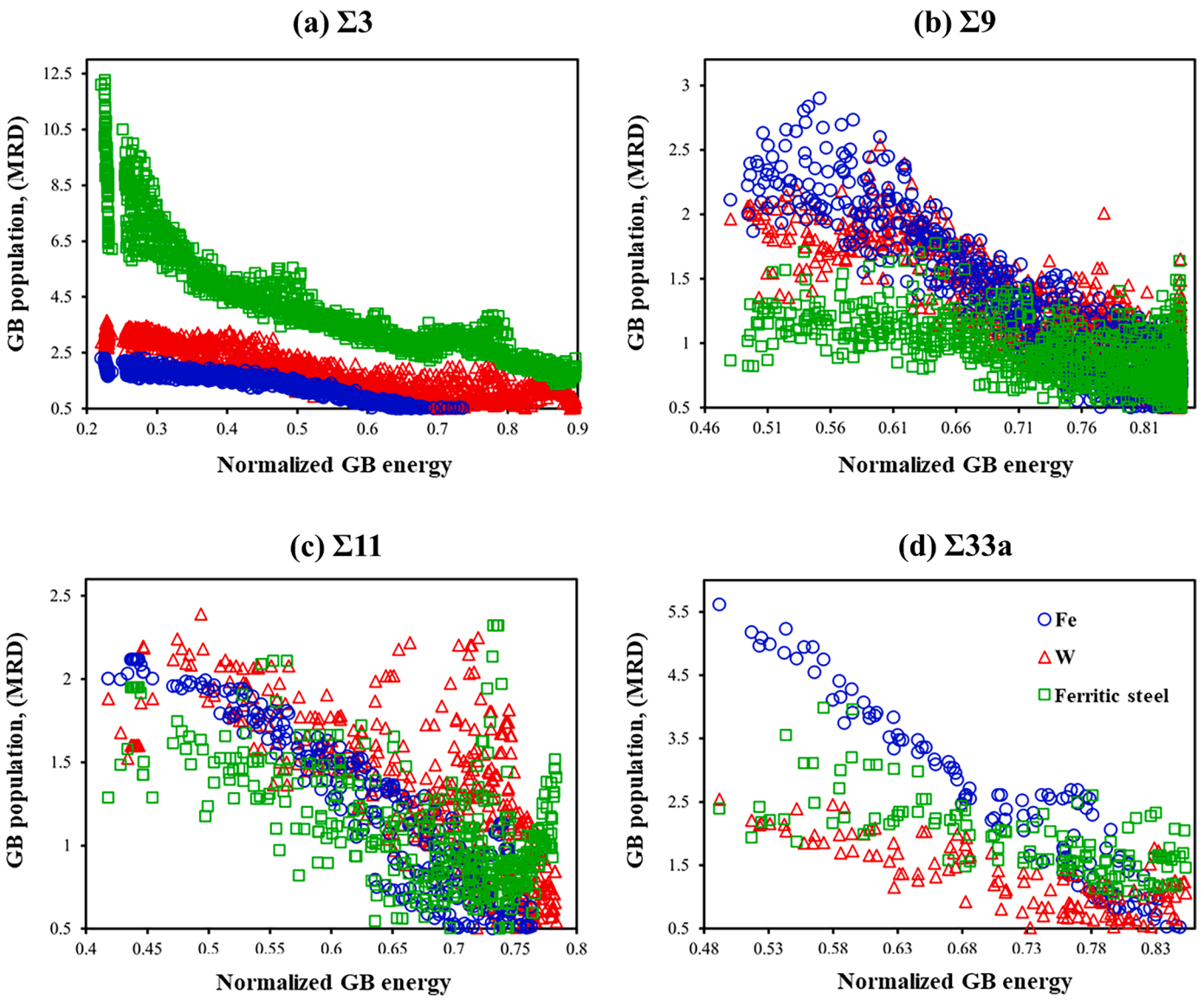

Fig. 5. Comparisons between the normalized GB energies and populations [39–41] for the **(a)** Σ3 60° <111>, **(b)** Σ9 38.94° <110>, **(c)** Σ11 50.48° <110>, and **(d)** Σ33a 20.05° <110> misorientations in Fe [39] (blue circles), W [40] (red triangles), and ferritic steel [41] (green squares). (For interpretation ofthe references to color in this figure legend, the reader is referred to the web version of this article.)

used for GBE of bcc metals.

Supplementary data

All data, including MATLAB scripts as well as the EAM-simulated and interpolated energies have been made available online at supplementary materials or at the GitHub repository (https://github.com/simdsci/uGBE_BCC).

Declaration of Competing Interest

The authors declare that they have no known competing financial interests or personal relationships that could have appeared to influence the work reported in this paper.

Acknowledgement

This research project is supported by Thailand Science Research and Innovation (TSRI), Basic Research Fund: Fiscal year 2023 under project number FRB660073/0164. O.C. acknowledges financial support by Petchra Pra Jom Klao Doctoral Scholarship, KMUTT and the Thailand Institute of Nuclear Technology (TINT). S.R. acknowledges the supports provided by the Thailand Science Research and Innovation (TSRI) under Fundamental Fund (Project: Advanced Materials and Manufacturing for Applications in New S-curve Industries), and the Research Strengthening Project of the Faculty of Engineering, King Mongkut's University of Technology Thonburi (KMUTT).

Supplementary materials

Supplementary material associated with this article can be found, in the online version, at doi:10.1016/j.scriptamat.2023.115821.

References

[1] S.Q. Cao, J.X. Zhang, J.S. Wu, J.G. Chen, Effects of GBCD on cold work embrittlement of high strength interstitial free steels, Mater. Des. 27 (2006) 53–57, https://doi.org/10.1016/j.matdes.2004.09.014.
[2] H. Yan, H. Bi, X. Li, Z. Xu, Effect of two-step cold rolling and annealing on texture, grain boundary character distribution and r-value of Nb+Ti stabilized ferritic

stainless steel, Mater. Charact. 60 (2009) 65–68, https://doi.org/10.1016/j.matchar.2008.05.006.
[3] J. Yang, L. Fan, J. Jia, R. Wu, X. Song, L. Jiang, Microtexture Evolution and Grain Boundary Character Distribution of Interstitial-Free Steels With Moderate Levels of Cold Rolling Reductions, J. Iron Steel Res. Int. 20 (2013) 47–52, https://doi.org/10.1016/S1006-706X(13)60215-0.
[4] D. Rath, P. Setia, N. Tripathi, S. Shekhar, Outstanding improvement in the CSL distribution in interstitial free (IF) steel via strain annealing route, Mater. Charact. 186 (2022), 111817, https://doi.org/10.1016/j.matchar.2022.111817.
[5] Y. Zhao, I.C. Cheng, M.E. Kassner, A.M. Hodge, The effect of nanotwins on the corrosion behavior of copper, Acta Mater 67 (2014) 181–188, https://doi.org/10.1016/j.actamat.2013.12.030.
[6] L. Lu, Y. Shen, X. Chen, L. Qian, K. Lu, Ultrahigh Strength and High Electrical Conductivity in Copper, Science 304 (2004) 422–426, https://doi.org/10.1126/science.1092905.
[7] T. Watanabe, Grain boundary engineering: historical perspective and future prospects, J. Mater. Sci. 46 (2011) 4095–4115, https://doi.org/10.1007/s10853-011-5393-z.
[8] V.Y. Gertsman, S.M. Bruemmer, Study of grain boundary character along intergranular stress corrosion crack paths in austenitic alloys, Acta Mater 49 (2001) 1589–1598, https://doi.org/10.1016/S1359-6454(01)00064-7.
[9] S. Gao, Z. Hu, M. Duchamp, P.S.S.R. Krishnan, S. Tekumalla, X. Song, M. Seita, Recrystallization-based grain boundary engineering of 316L stainless steel produced via selective laser melting, Acta Mater 200 (2020) 366–377, https://doi.org/10.1016/j.actamat.2020.09.015.
[10] M. Laleh, A.E. Hughes, M.Y. Tan, G.S. Rohrer, S. Primig, N. Haghdadi, Grain boundary character distribution in an additively manufactured austenitic stainless steel, Scr. Mater. 192 (2021) 115–119, https://doi.org/10.1016/j.scriptamat.2020.10.018.
[11] S.Echeverri Restrepo, S. Tamayo Giraldo, B.J. Thijsse, Using artificial neural networks to predict grain boundary energies, Comput. Mater. Sci. 86 (2014) 170–173, https://doi.org/10.1016/j.commatsci.2014.01.039.
[12] S.G. Baird, E.R. Homer, D.T. Fullwood, O.K. Johnson, Five degree-of-freedom property interpolation of arbitrary grain boundaries via Voronoi fundamental zone framework, Comput. Mater. Sci. 200 (2021), 110756, https://doi.org/10.1016/j.commatsci.2021.110756.
[13] H. Zheng, X.-G. Li, R. Tran, C. Chen, M. Horton, D. Winston, K.A. Persson, S.P. Ong, Grain boundary properties of elemental metals, Acta Mater 186 (2020) 40–49, https://doi.org/10.1016/j.actamat.2019.12.030.
[14] R. Sarochawikasit, C. Wang, P. Kumam, H. Beladi, T. Okita, G.S. Rohrer, S. Ratanaphan, Grain boundary energy function for α iron, Materialia 19 (2021), 101186, https://doi.org/10.1016/j.mtla.2021.101186.
[15] O. Chirayutthanasak, R. Sarochawikasit, A. Wisitsorasak, N. Rujisamphan, T. Frolov, T. Oppelstrup, S. Dangtip, G.S. Rohrer, S. Ratanaphan, Anisotropic grain boundary area and energy distributions in tungsten, Scr. Mater. 209 (2022), 114384, https://doi.org/10.1016/j.scriptamat.2021.114384.
[16] W. Ye, H. Zheng, C. Chen, S.P. Ong, A Universal Machine Learning Model for Elemental Grain Boundary Energies, Scr. Mater. 218 (2022), 114803, https://doi.org/10.1016/j.scriptamat.2022.114803.
[17] B. Waters, D.S. Karls, I. Nikiforov, R.S. Elliott, E.B. Tadmor, B. Runnels, Automated determination of grain boundary energy and potential-dependence using the OpenKIM framework, Comput. Mater. Sci. 220 (2023), 112057, https://doi.org/10.1016/j.commatsci.2023.112057.
[18] B. Runnels, I.J. Beyerlein, S. Conti, M. Ortiz, An analytical model of interfacial energy based on a lattice-matching interatomic energy, J. Mech. Phys. Solids. 89 (2016) 174–193, https://doi.org/10.1016/j.jmps.2016.01.008.
[19] S. Ratanaphan, D.L. Olmsted, V.V. Bulatov, E.A. Holm, A.D. Rollett, G.S. Rohrer, Grain boundary energies in body-centered cubic metals, Acta Mater 88 (2015) 346–354, https://doi.org/10.1016/j.actamat.2015.01.069.
[20] V.V. Bulatov, B.W. Reed, M. Kumar, Grain boundary energy function for fcc metals, Acta Mater 65 (2014) 161–175, https://doi.org/10.1016/j.actamat.2013.10.057.
[21] S. Ratanaphan, T. Boonkird, R. Sarochawikasit, H. Beladi, K. Barmak, G.S. Rohrer, Atomistic simulations of grain boundary energies in tungsten, Mater. Lett. 186 (2017) 116–118, https://doi.org/10.1016/j.matlet.2016.09.104.
[22] M.I. Mendelev, S. Han, D.J. Srolovitz, G.J. Ackland, D.Y. Sun, M. Asta, Development of new interatomic potentials appropriate for crystalline and liquid iron, Philos. Mag. 83 (2003) 3977–3994, https://doi.org/10.1080/14786430310001613264.
[23] Y. Li, D.J. Siegel, J.B. Adams, X.-Y. Liu, Embedded-atom-method tantalum potential developed by the force-matching method, Phys. Rev. B. 67 (2003), 125101, https://doi.org/10.1103/PhysRevB.67.125101.
[24] M.W. Finnis, J.E. Sinclair, A simple empirical N-body potential for transition metals, Philos. Mag. A. 50 (1984) 45–55, https://doi.org/10.1080/01418618408244210.
[25] X.W. Zhou, H.N.G. Wadley, R.A. Johnson, D.J. Larson, N. Tabat, A. Cerezo, A. K. Petford-Long, G.D.W. Smith, P.H. Clifton, R.L. Martens, T.F. Kelly, Atomic scale structure of sputtered metal multilayers, Acta Mater 49 (2001) 4005–4015, https://doi.org/10.1016/S1359-6454(01)00287-7.
[26] S.J. Plimpton, LAMMPS: Large-scale Atomic/Molecular Massively Parallel Simulator, Sandia National Laboratories, 2007.
[27] M.R. Fellinger, H. Park, J.W. Wilkins, Force-matched embedded-atom method potential for niobium, Phys. Rev. B. 81 (2010), 144119, https://doi.org/10.1103/PhysRevB.81.144119.
[28] S.R. Wilson, K.G.S.H. Gunawardana, M.I. Mendelev, Solid-liquid interface free energies of pure bcc metals and B2 phases, J. Chem. Phys. 142 (2015), 134705, https://doi.org/10.1063/1.4916741.
[29] A. Nichol, G.J. Ackland, Property trends in simple metals: An empirical potential approach, Phys. Rev. B. 93 (2016), 184101, https://doi.org/10.1103/PhysRevB.93.184101.
[30] D. Wolf, A read-shockley model for high-angle grain boundaries, Scr. Metall. 23 (1989) 1713–1718, https://doi.org/10.1016/0036-9748(89)90348-7.
[31] C. Li, S. Lu, S. Divinski, L. Vitos, Theoretical and experimental grain boundary energies in body-centered cubic metals, Acta Mater 255 (2023), 119074, https://doi.org/10.1016/j.actamat.2023.119074.
[32] D. Scheiber, R. Pippan, P. Puschnig, L. Romaner, Ab initio calculations of grain boundaries in bcc metals, Model. Simul. Mater. Sci. Eng. 24 (2016), 035013, https://doi.org/10.1088/0965-0393/24/3/035013.
[33] X.-R. Zheng, X.-S. Kong, X. Li, X. Li, Y. Zhang, Y. Xu, X. Wu, C.S. Liu, Ab initio calculations and empirical potential assessments of the energy and structure of symmetric tilt grain boundaries in tungsten, Comput. Mater. Sci. 229 (2023), 112446, https://doi.org/10.1016/j.commatsci.2023.112446.
[34] M.I. Mendelev, S. Han, W. Son, G.J. Ackland, D.J. Srolovitz, Simulation of the interaction between Fe impurities and point defects in V, Phys. Rev. B. 76 (2007), 214105, https://doi.org/10.1103/PhysRevB.76.214105.
[35] Y. Shiihara, R. Kanazawa, D. Matsunaka, I. Lobzenko, T. Tsuru, M. Kohyama, H. Mori, Artificial neural network molecular mechanics of iron grain boundaries, Scr. Mater. 207 (2022), 114268, https://doi.org/10.1016/j.scriptamat.2021.114268.
[36] J. Wang, G.K.H. Madsen, R. Drautz, Grain boundaries in bcc-Fe: a density-functional theory and tight-binding study, Model. Simul. Mater. Sci. Eng 26 (2018), 025008, https://doi.org/10.1088/1361-651X/aa9f81.
[37] T. Frolov, W. Setyawan, R.J. Kurtz, J. Marian, A.R. Oganov, R.E. Rudd, Q. Zhu, Grain boundary phases in bcc metals, Nanoscale 10 (2018) 8253–8268, https://doi.org/10.1039/C8NR00271A.
[38] S. Kobayashi, W. Yang, Y. Tomobe, R. Okada, S. Tsurekawa, Low-angle boundary engineering for improving high-cycle fatigue property of 430 ferritic stainless steel, J. Mater. Sci. 55 (2020) 9273–9285, https://doi.org/10.1007/s10853-020-04555-0.
[39] S. Ratanaphan, Grain Boundary Character Distributions in Isostructural Materials, PhD Thesis Dep, Mater. Sci. Eng. Carnegie Mellon Univ. (2013).
[40] X. Liu, D. Choi, H. Beladi, N.T. Nuhfer, G.S. Rohrer, K. Barmak, The five-parameter grain boundary character distribution of nanocrystalline tungsten, Scr. Mater. 69 (2013) 413–416, https://doi.org/10.1016/j.scriptamat.2013.05.046.
[41] H. Beladi, G.S. Rohrer, The relative grain boundary area and energy distributions in a ferritic steel determined from three-dimensional electron backscatter diffraction maps, Acta Mater 61 (2013) 1404–1412, https://doi.org/10.1016/j.actamat.2012.11.017.
[42] E.A. Holm, G.S. Rohrer, S.M. Foiles, A.D. Rollett, H.M. Miller, D.L. Olmsted, Validating computed grain boundary energies in fcc metals using the grain boundary character distribution, Acta Mater 59 (2011) 5250–5256, https://doi.org/10.1016/j.actamat.2011.05.001.
[43] E.R. Homer, G.L.W. Hart, C. Braxton Owens, D.M. Hensley, J.C. Spendlove, L. H. Serafin, Examination of computed aluminum grain boundary structures and energies that span the 5D space of crystallographic character, Acta Mater 234 (2022), 118006, https://doi.org/10.1016/j.actamat.2022.118006.
[44] D. Scheiber, O. Renk, M. Popov, L. Romaner, Temperature dependence of surface and grain boundary energies from first principles, Phys. Rev. B. 101 (2020), 174103, https://doi.org/10.1103/PhysRevB.101.174103.
[45] S.M. Foiles, Temperature dependence of grain boundary free energy and elastic constants, Scr. Mater. 62 (2010) 231–234, https://doi.org/10.1016/j.scriptamat.2009.11.003.
[46] S. Ratanaphan, R. Sarochawikasit, N. Kumanuvong, S. Hayakawa, H. Beladi, G. S. Rohrer, T. Okita, Atomistic simulations of grain boundary energies in austenitic steel, J. Mater. Sci. 54 (2019) 5570–5583, https://doi.org/10.1007/s10853-018-03297-4.
[47] N. Sakaguchi, M. Endo, S. Watanabe, H. Kinoshita, S. Yamashita, H. Kokawa, Radiation-induced segregation and corrosion behavior on Σ3 coincidence site lattice and random grain boundaries in proton-irradiated type-316L austenitic stainless steel, J. Nucl. Mater. 434 (2013) 65–71, https://doi.org/10.1016/j.jnucmat.2012.11.036.
[48] Y. Yang, S. Schönecker, W. Li, C. Wang, S. Huang, J. Zhao, L. Vitos, First-principles study of the Σ3(112) grain boundary in Fe-rich Fe-Cr alloys, Scr. Mater. 181 (2020) 140–143, https://doi.org/10.1016/j.scriptamat.2020.02.029.
[49] S.J. Dillon, M.P. Harmer, G.S. Rohrer, The Relative Energies of Normally and Abnormally Growing Grain Boundaries in Alumina Displaying Different Complexions, J. Am. Ceram. Soc. 93 (2010) 1796–1802, https://doi.org/10.1111/j.1551-2916.2010.03642.x.
[50] S.A. Bojarski, M. Stuer, Z. Zhao, P. Bowen, G.S. Rohrer, Influence of Y and La Additions on Grain Growth and the Grain-Boundary Character Distribution of Alumina, J. Am. Ceram. Soc. 97 (2014) 622–630, https://doi.org/10.1111/jace.12669.
[51] M.N. Kelly, S.A. Bojarski, G.S. Rohrer, The temperature dependence of the relative grain-boundary energy of yttria-doped alumina, J. Am. Ceram. Soc. 100 (2017) 783–791, https://doi.org/10.1111/jace.14488.
[52] E.A. Holm, D.L. Olmsted, S.M. Foiles, Comparing grain boundary energies in face-centered cubic metals: Al, Au, Cu and Ni, Scr. Mater. 63 (2010) 905–908, https://doi.org/10.1016/j.scriptamat.2010.06.040.